Universidad Nacional Autónoma de México

Facultad de Ciencias

Construction and Application of a Neutral Particle Detector for experiments on Spectroscopy of Negative Ions

T E S I S

que presenta:

Morales Rodríguez Andrea

Que para obtener el título de:

Física

Tutor:

Dr. Remigio Cabrera Trujillo

Ciudad Universitaria, CD.MX. 2024

"The only person you're truly competing against, is yourself."
— J.L Picard, *Star Trek: The Next Generation, "Coming of Age".*

Acknowledgements

I would like to acknowledge and express my gratitude to all the people that guided and supported me throughout this process. First and foremost, to Professor Cabrera, the first one to believe in me and who offered me this amazing learning opportunity. Professor Hanstorp, who made this opportunity possible, guided and watched over me, who was always ready to offer advice. Dr. Leimbach, who lent me advice in regards to experimental work and thesis writing, who also had the patience to answer all my questions and explain everything I needed to know. Annie, who was always willing to help me especially during hard times. José, a friend that always heartedly adviced me and motivated me as my older brother whenever I needed it. Pablo, Bere, María and Dani, that were always there for me and made this time unforgettable. Olle, the one who waltzed into my life when I needed him the most, and has incessantly supported and cheered me through this time. Last but not least, to my family, the ones that were sure I was going to make it through this even before I did.

Abstract

Anions, also called negative ions, are a negatively charged version of the different elements present in the periodic table and are relevant to study due to them being sensitive probes of electron correlation, which is necessary for the accurate understanding of atomic systems. Since the early 20th century, the existence of charged atoms, including negative ions, has been extensively studied, both theoretically and experimentally. The most commonly used experimental technique in the investigation of negative ions, laser photodetachment threshold spectroscopy (LPTS), yields two final products: a neutral atom and a free electron. Monitoring the production of electrons or neutral atoms can provide a comprehensive insight into the photodetachment process by expanding the amount of information acquired from these experiments. Neutral atom monitoring can be performed using a neutral particle detector (NPD), where atoms impinging on a graphene coated quartz target produce secondary electrons that are subsequently guided to a channel electron multiplier (CEM), where the signal is collected. This thesis deals with the design, construction, and testing of an NPD for use at the Rydberg atom detector for anion research (RADAR) beamline in the Gothenburg University Negative Ion Laser Laboratory (GUNILLA) aimed to broaden the monitoring range of the experiments performed in this beamline. Additionally, the design and simulation of a testing chamber for CEMs is proposed. Finally, an experiment to measure the electron affinity of ^{85}Rb was performed, where it was determined to be 485.894(8)meV, enhancing precision by an order of magnitude over prior measurements.

Notation

This section compiles a glossary of the acronyms used along this thesis to facilitate further reading and referencing. In the text, the acronyms are defined once.

NPD - Neutral Particle Detector

EA - Electron Affinity

CEM - Channel Electron Multiplier

RADAR - Rydberg Atom Detector for Anion Research

GUNILLA - Gothenburg University Negative Ion Laser LAboratory

RIS - Resonant Ionization Spectroscopy

AMS - Acceleration Mass Spectrometry

LPD - Laser PhotoDetachment

OPO - Optical Parametric Oscillator

MCP - MicroChannel Plate

PSD - Position Sensitive Detector

Contents

List of Figures

Chapter 1

Introduction

In 1897, Sir J.J. Thomson broke the concept of the atom as a single homogeneous particle with his discovery of the electron through his work with cathode rays. A few years later, he continued the work refining mass spectrometry methods previously developed by W. Wien. These experiments allowed him to separate particles by their charge to mass ratio and visualize them using a photographic plate. This work led Thomson to identify both positive and negatively charged atoms and molecules [1].

Years later, Wildt attributed the atomic negative hydrogen ions presence to the deviation from the typical black-body curve in the continuous solar spectrum. This was based on the already established knowledge of free electrons and the abundance of hydrogen in the sun. Although Wildt's theory was supported theoretically [2], measurements of the binding energies had not yet been determined for most of the known elements. This led to the first tests of negative ion beam production by W.L. Fite, which culminated in a DC glow discharge source [3]. The construction of this source lead to the first recorded photodetachment experiment carried out in 1953 [4]. Two years later, the photodetachment cross sections for hydrogen and deuterium anions were measured by Branscomb and Smith [5]. These experiments have been updated and repeated for a vast number of elements.

Anions primarily arise from polarization effects, although they can also result from other interactions such as electron transfer and chemical bonding. This leads to increased significance of Coulomb repulsion among electrons in these interactions. Therefore, negative ions represent a great benchmark for the study of electron correlations and strongly correlated systems, in general. This is further explored in Chapter 2.

The electron affinity (EA) is defined as the amount of energy liberated when an electron is attached to a neutral atomic system, forming a negatively charged ion. The EA can be measured using spectroscopic techniques, where the photon energy of a laser is varied over the threshold for the photodetachment process [6, 7]. Neutral atoms are generated as a result of laser photodetachment when a beam of anions

is exposed. The laser removes electrons from the anions, resulting in the formation of neutral atoms. [8, 9].

The photodetachment process can be monitored by secondary emission detectors that record neutral atom production [10, 11]. These detectors receive the neutral atoms, which impinge on the target surface causing the creation of secondary electrons that can be detected by a Channel Electron Multiplier (CEM) [12, 13, 14].

Other techniques that have been developed over the years to better utilize photodetachment processes include the proposal [15] and application of a photoionization microscope, which not only assists in electron affinity (EA) measurements but also aids in the analysis of fine structures, as demonstrated in [16].

Another explored technique [17] involves the use of the Double ElectroStatic Ion-Ring Experiment (DESIREE), where ion beams are stored in two electrostatic ion rings at cryogenic temperatures. By carefully controlling the voltages applied to the rings, the experiment achieved the simultaneous storage of positive and negative ion beams, enabling the study of ion-neutral collisions. These facilities have housed numerous related experiments on the study of negative ions, including the high-precision measurement of oxygen [18]. Current EA values can be found in reviews such as [19, 20, 16, 18, 21], and a more recent collection of the measured values can be found in [22].

Negative ions are also of interest in a variety of other fields. An example is the presence of anions in space, where H^- plays a huge role for astrophysics: The bound-free transitions in this anion are remarkably present in the opacity of the visible region of the electromagnetic spectrum of stars with relatively low photospheric temperatures (i.e. less than 7000 K) as firstly described by Wildt in his observation of the solar spectrum. Likewise, the H^- anion is ought to play a critical role in the early stages of the Universe, contributing to molecular hydrogen formation [23]. This newly formed molecular hydrogen would expand and eventually collapse, forming stellar objects and protogalaxies, further allowing the creation of heavier elements through nucleosynthesis [24]. In addition, the detection of anions in stellar atmospheres and comet tails has been found to be of relevance for better understanding of the numerous chemical reactions sustained in stars and interstellar media, although the need for more high-resolution data of the rotational spectra for anions has been remarked [24, 25]. This information is needed for the correct identification of some abundant species, where no previous data has been recorded [23, 26, 25].

In this work, a Neutral Particle Detector (NPD) was developed and integrated into the Rydberg Atom Detector for Anion Research (RADAR) at GUNILLA (Gothenburg University Negative Ion Laser LAboratory) based on a previous design [11]. By incorporating the NPD, it is aimed to expand the scope of monitoring of the interactions that take place during photodetachment experiments. The high sensitivity offered by the NPD will enable RADAR to serve as a standard beamline for all laser photodetachment

experiments conducted at GUNILLA.

Furthermore, a test chamber was designed, which includes an electron beam apparatus for testing particle detectors. This chamber not only allows to evaluate the performance of the desired NPD but also facilitates testing of various types and components of particle detectors utilized at GUNILLA. Through this testing process, we can ensure the long-term functionality of the detectors without disrupting the experimental beam time.

As a final point, this work presents an updated determination of the electron affinity of rubidium through the measurement of the partial photodetachment cross section of the negative ion, resulting in the residual atom being in the $^5P_{3/2}$ excited state. By utilizing resonance ionization spectroscopy, state selectivity was achieved and accurately measured the Wigner s-wave threshold onset of photodetachment, leading to a significantly improved value of 485.894(8) meV for the electron affinity of rubidium, surpassing previous measurements by an order of magnitude.

Chapter 2

Theoretical Framework

2.1 Negative Ions

While the Coulomb force doesn't attract electrons to neutral atoms, their mutual proximity can polarize the atom's electron cloud, inducing an electric dipole moment. This induced effect is responsible for binding the free electron, endowing the existence of negative ions. This process is dependent upon the polarizability of the species in question. There are other possible mechanisms that result in the creation of anions, such as collision dissociation and charge transfer in collisions. The details of these mechanisms lay beyond the scope of this work. The energy obtained by the atom in this binding process is referred to as the Electron Affinity (EA) of the neutral atom. Hence, this energy is defined as

$$EA(X) = E(X) - E(X^-). \tag{2.1}$$

Equation (2.1) represents the condition for a stable negative ion if the resulting EA is positive. The nature of the interaction of the free electron with an atom, as described, implies that the negative ion is a fragile system with binding energies typically in the order of one eV. This short-term interaction is discussed later in this text.

Predictions from the EA can be drawn by examining the periodic table (see Figure 2.1) and the electronic shell filling of elements. This provides insight into what to anticipate when it comes to anions. Alkaline-earth materials, for example, possesses a low or negative EA as the extra electron must occupy a new subshell, leading to unstable negative ions. Meanwhile, for halogens, the extra electron completes a shell and therefore, those are the elements with the highest EA.

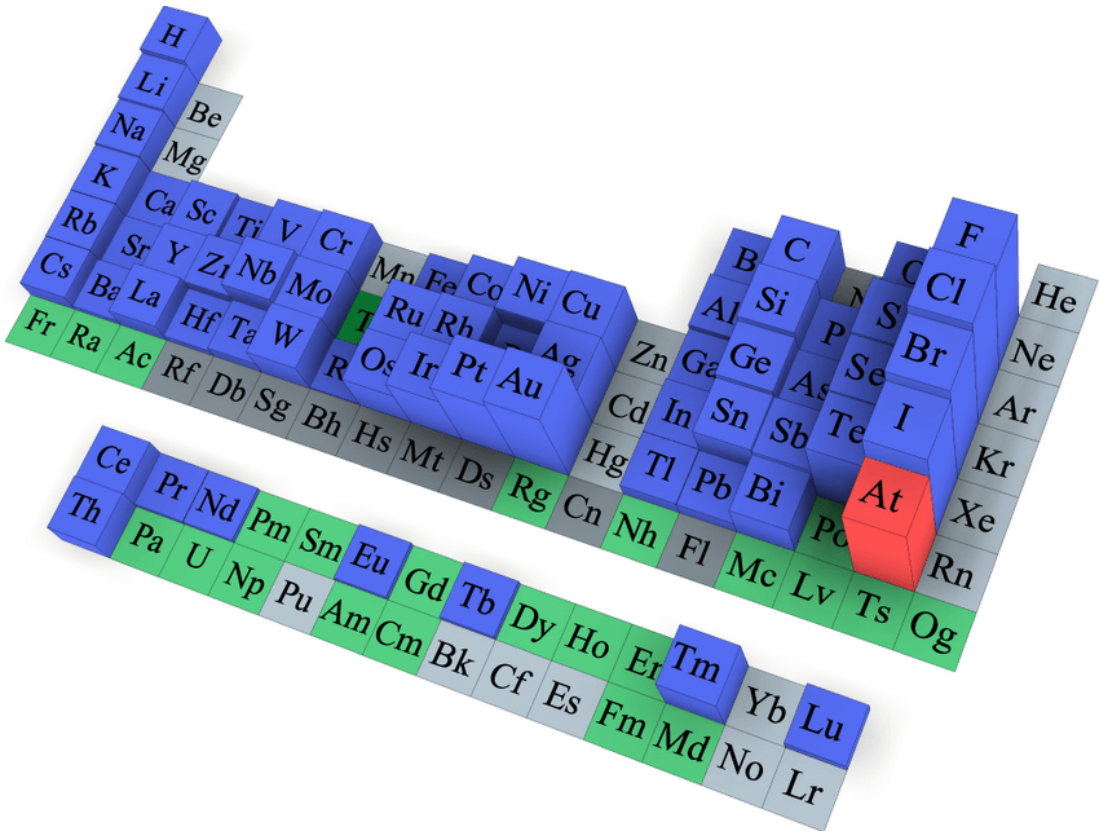

Figure 2.1: Periodic table portraying the EA of the elements. The height corresponds to the measured value. The elements that are predicted theoretically to form stable anions are shown in green, and the elements predicted as unstable anions are shown in gray. The elements with experimentally measured EA are marked in blue. Extracted from [27].

2.2 Photodetachment process

If the energy of an incoming photon γ is sufficiently high when absorbed by an anion, the photodetachment process can occur:

$$X^- + \gamma \longrightarrow X + e^-. \tag{2.2}$$

This process can be observed by the absorption of photons, detached electrons, or neutral atoms. This monitoring provides information about the structure of the negative ion and the corresponding neutral atom by relating the detected signal to photon energy. Photodetachment occurs only if an incoming photon has energy equal to or greater than the EA of a given anion X^-. The probability of this process to occur is expressed as a cross section σ. In general, the probability of a transition from the initial state to the final continuum state due to the interaction between an atom and a photon is described by Fermi's golden rule [28]:

$$P_d = \frac{2\pi}{\hbar} \mid \langle \varphi_f \mid D \mid \varphi_i \rangle \mid^2 \rho_f, \tag{2.3}$$

where D is the electric dipole coupling operator corresponding to photoabsorption, $\hbar$ the reduced Planck constant, ρ_f is the density of the final states in the continuum and $\varphi_{f,i}$ are the wavefunctions of the final and initial states, respectively. The density ρ_f is proportional to the energy of the free electron $\mathcal{E}$:

$$\rho_f \propto (\mathcal{E})^{1/2}. \tag{2.4}$$

After the photodetachment process, the interaction between the free electron and the residual atom can be described by the effective potential

$$V_{eff}(r) = \frac{-\alpha}{r^4} + \frac{\hbar^2}{2\mu r^2} l(l+1), \tag{2.5}$$

where α is the polarizability of the system, the first term is the induced dipole potential and the second term is the centrifugal barrier of the potential. Here l is the angular momentum of the outgoing electron, μ is the reduced mass and r is the distance between the electron and the nuclei of the residual atom.

From equation (2.5), one can observe that at a large r, the centrifugal term dominates as the first term decays faster. Subsequently, based on Fermi's golden rule [Eq.(2.3)]one finds that

$$\sigma \propto k^{2l+1}, \tag{2.6}$$

where k is the linear momentum and l the orbital momentum of the resulting electron from the photodetachment process. This is referred to as Wigner's threshold law, rigorously treated in Eugene Wigner's article [8].

From equation (2.6)one obtains

$$\sigma(E) \propto (E_{ph} - E_{th})^{l+1/2}, \tag{2.7}$$

where E_{ph} is the energy of the photon, E_{th} is the threshold energy and l the orbital quantum number of the emitted electron.

This cross section near the threshold can be described in terms of energy:

$$\sigma(E) \propto \begin{cases} a & \text{for } E_{ph} \leq \text{EA} \\ a + b(E_{ph} - \text{EA})^{l+\frac{1}{2}} & \text{for } E_{ph} > \text{EA}. \end{cases} \tag{2.8}$$

This equation shows that when the angular momentum of the ejected electron is zero, the cross section as a function of photon energy follows an s-wave behavior, characterized by a square-root relationship. On the other hand, according to the selection rule $\Delta l = \pm 1$, if the photodetachment process does not involve any other excitation, the additional angular momentum is carried away by the ejected electron, resulting in a different cross section behavior known as a p-wave. Both types of onsets are illustrated in figure 2.2. In theory, a should be zero, but during the experiments, this value is referred to as the background.

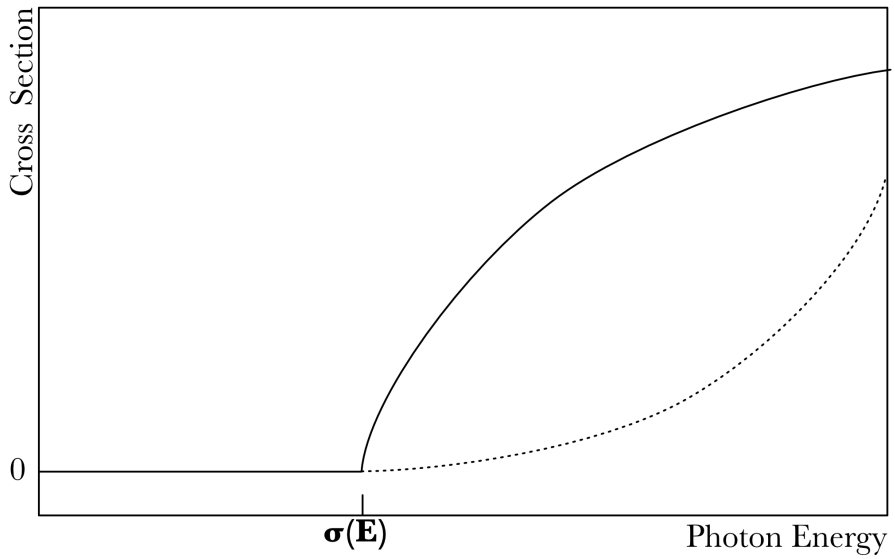

Figure 2.2: Plot of the photodetachment cross section shape close to threshold comparing s-wave (solid line) and p-wave behavior (dotted line).

The sharp onset of the s-wave cross section behavior allows a much more precise determination of the EA compared to the onset from the p-wave, as seen in figure 2.2. Hence, for certain elements, (e.g. rubidium) a RIS technique can offer higher spectroscopic resolution than other photodetachment techniques. This is explained further in the EA of Rubidium section.

The EA of atoms can be determined using various methods. The most accurate method is based on the photodetachment of negative ions using laser radiation [6].

2.3 Experimental Methods of photodetachment

The invention of the laser presented the prospect of a more exact way of performing photodetachment experiments and spectroscopy, in general. Its properties, such as the large spectral power density, small divergence of collimated beams, small spectral linewidth, narrow-band wavelength tuning and possibility for pulsed or mode-locked lasing represented a new opportunity to obtain higher resolution and more controlled measurements compared to those with other types of light sources [29]. The elements of a laser can be reduced to three components [29]: The **active medium**, that amplifies the incident electromagnetic

wave; the **energy pump** that generates a population inversion in the active medium; and the **optical resonator**, that is comprised of two opposite mirrors fixed to store part of the induced emission along with some resonating modes.

From the incorporation of the laser to the spectroscopy studies, some techniques were refined, such as Laser Photodetachment Threshold Spectroscopy (LPTS).

2.3.1 Laser photodetachment threshold spectroscopy

In LPTS, the incoming photon energy is varied over the threshold region of photodetachment. The detached electrons or the residual neutral atoms are subsequently detected. The yield of photodetachment signal as a function of photon energy is obtained and fitted to the previously discussed Wigner law. From this fit, both the threshold for photodetachment and its behavior can be studied. Different laser geometries can be arranged to interact with the ion beam: **cross-beam**, where the laser interacts with the ion beam at ideally, exactly 90°; and **collinear**, where the laser ideally overlaps the beam and is switched from copropagating to counterpropagating with respect to the direction of the accelerated beam. The selection of the geometry is strongly correlated to the purpose of the experiment.

Let ω be the frequency of light, the velocity of ions ν and the interception angle θ of the laser and ion beam. Then, the relativistic Doppler shift is given by [9]:

$$\omega' = \omega \frac{1 - \frac{\nu}{c_0} cos(\theta)}{\sqrt{1 - \frac{\nu^2}{c_o^2}}}. \tag{2.9}$$

From this equation, one can see that if the angle between the laser and the ion beam is exactly 90°as intended in a cross-beam arrangement, the LPTS experiment would then have a Doppler-free photodetachment threshold. Nevertheless, in practice, this kind of measurements are limited in resolution due to the divergence of both laser and ion beam. This divergence induces a Doppler shift, that is directly responsible for limiting resolution, as previously stated.

For low resolution experiments, it is enough to correct the value by using the ion beam velocity [9]. For high-resolution experiments, both copropagating and counterpropagating geometries have to be involved, setting $\theta = 0$ and accounting for Doppler shift by simply taking the geometric mean of both geometries. Additionally, performing two-photon photodetachment with a high power laser is recommended to achieve high-resolution results. [9, 30, 31].

2.3.2 Resonance Ionization Spectroscopy

The interaction of gas-phase atoms with multiple photons is the basis of RIS. A photon with a wavelength λ_1 from one laser that is overlapped with an ion beam will excite an atom from its ground state to a bound intermediate electronic state. From a second overlapped laser, a photon of wavelength λ_2 further excites this atom from an intermediate state to above its ionization potential. This process results in electron emission and thus ionization of the neutral atom, as depicted in figure (2.3).

This technique was first explored by Hurst [32], in which the excited states of helium were explored and single-atom analysis was shown to be possible, proving RIS to be a highly selective and sensitive method. In general, this process may be helpful in positive-ion generation from a neutral atom beam, resulting in cations and free electrons [33].

Other applications of RIS include measurements of photoionization cross sections for excited states and the detection of single atoms in individual ionization tracks [34, 35].
The photodetachment process, which measures cross sections and provides insights into negative ions, faces challenges related to sensitivity and selectivity. These challenges arise from decreased overlap between initial and final state wave functions and the presence of multiple open decay channels. To address these issues, researchers have modified the experimental setup, such as using a collinear laser-ion beam configuration, to enhance sensitivity through increased interaction regions [36]. However, achieving selectivity for individual photodetachment channels remains a goal. Resonant Ionization Spectroscopy (RIS) has proven beneficial in experiments requiring highly excited residual atoms, as it offers final state specificity.

Furthermore, a different approach involving the use of two lasers has been explored to measure the threshold for both s-wave and p-wave photodetachment [13]. RIS, being highly efficient in detecting ions and electrons, surpasses photon detection in sensitivity [37], with the possibility of approaching near 100 percent efficiency in resonant ionization of atoms [35].

The use of RIS in negative ion spectroscopy offers distinct advantages, primarily its high sensitivity in detecting atoms produced during the photodetachment process. This sensitivity enables selective investigation of relatively weak processes or cases involving excess photon channels. By applying this meticulous technique to negative ion spectroscopy, the ability to study the structural and dynamic properties of various anion states and their resonant transitions is opened with an unprecedented level of sensitivity. This potential has been further discussed and supported in studies such as [33, 34].

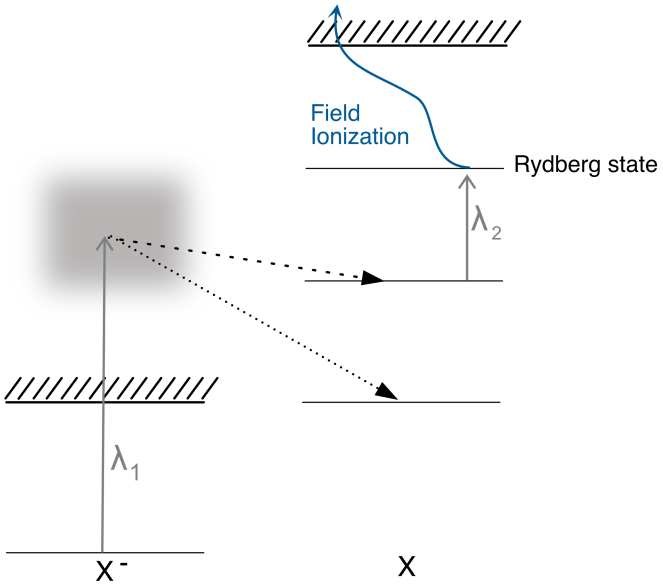

Figure 2.3: Energy level diagram of the process of RIS for negative ions as used in this thesis. A negative ion that is photodetached by interacting with a photon of wavelength λ_1 and opening the possibility of both s or p channels. Then, a photon of wavelength λ_2 is absorbed by the excited electron and propelled to a Rydberg excited state from the neutral atom. Finally, the atom is field ionized.

Chapter 3

Methodology

3.1 GUNILLA

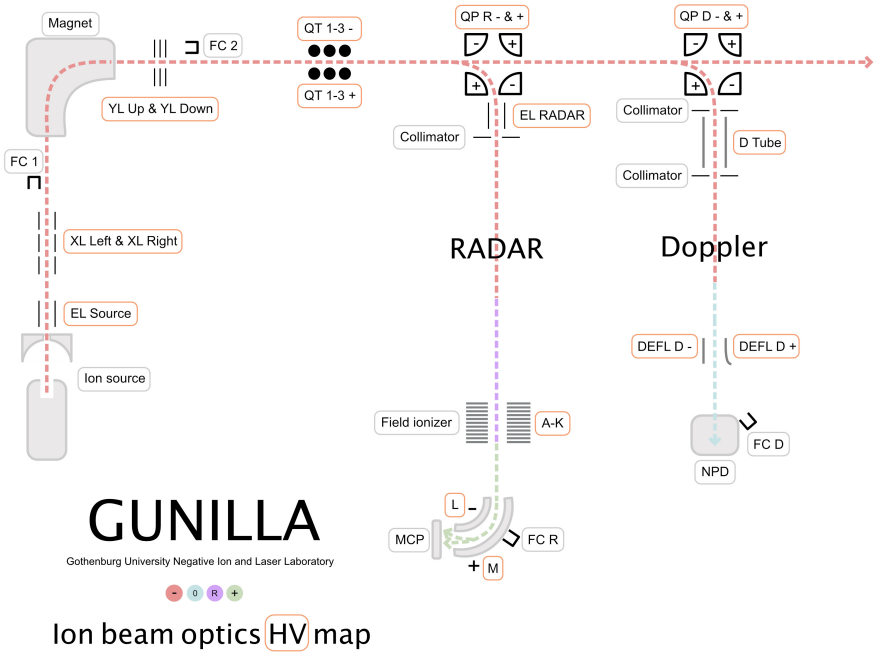

Figure 3.1: Diagram of GUNILLA. This diagram depicts the possible routes the ion beam can take, and some of its components. The ion beam path starts at the ion source, passes by an Einzel Lens. Then, continues through a deflector (XL left and right) that allows to control the orientation of the ion beam in the x-plane. The magnet bends the beam by 90°, which then passes another deflector in y-plane (YL up and down). Thereafter, the beam is focused again by the electrostatic quadrupole triplet (QT 1-3±) and introduced to the first quadrupole deflector (QP R ±). If this last electrostatic element is set to a certain voltage, the beam is bent 90° into the RADAR beamline. For the ion beam to reach the doppler beamline, this last deflector is then turned off and guided towards the next quadrupole deflector (QP D ±) that will then bend it and guide it to the beamline. Diagram courtesy of M. Nichols.

The Gothenburg University Negative Ion Laser LAboratory (GUNILLA), shown schematically in figure

3.1, is an ion beam facility consisting of a negative ion source, an electromagnetic mass separator and several experimental beamlines. Equipped with multiple detectors, experiments such as the measurement of electron affinities and photodetachment cross sections can be performed. The ion source at GUNILLA can, in principle, produce anions from any element able to form stable negative ions. The ion beam at GUNILLA is generated and subsequently mass separated. Then, ion species of interest are then guided by electrostatic elements into one of the two experimental beamlines: the Doppler chamber and the Rydberg Atom Detector for Anion Research (RADAR), as shown in figure 3.1 and further explained in this chapter.

3.1.1 Ion source

The ion source in use at GUNILLA is a Cs sputter source originally designed by Middleton [38] for Accelerator Mass Spectrometry (AMS). The ion source starts at a solid caesium reservoir that is heated up to about 100°C, administering Cs vapor between a cylindrical, hollow aluminum rod that works as a cathode and a curved surface, where the vapor is ionized. The cathode is previously prepared with a chemical solid compound that contains the desired atom species. Then, the positive Cs ions are accelerated onto the cathode and a caesium monolayer forms on the cathode surface from the ions emitted by the Cs oven. This monolayer interacts with sputtering fragments from the cathode, creating negative ions. Subsequently, these newly formed anions are accelerated towards the ionizer and transmitted through a hole, extracted using a total energy of 6 kV. The structure of the source and the sputtering process is illustrated in figure 3.2.

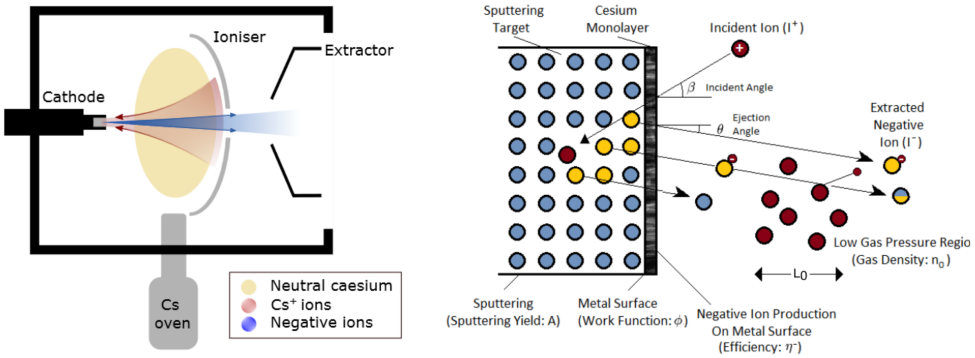

Figure 3.2: Schematics of the sputter source found in GUNILLA. On the right, the trajectory of the emerging ion beam is shown, along the geometries of the cathode and the reservoir, also called Cs oven. The sputtering process is shown on the left, depicting the formation and interaction of the Cs monolayer. Diagram courtesy of D. Leimbach.

3.1.2 Ion beam transport

After leaving the source, the ion beam is guided through the apparatus to one of the two experimental chambers mentioned before: Doppler or RADAR. This is achieved using several elements along the path

to focus and bend the beam. Among the optical elements guiding the beam, we can find:

Einzel Lens. A cylindrical component that is divided into three segments, where the outer rings are at the same potential, while the inner ring is set to a different voltage to focus the beam. The beam focusing is shown in figure 3.3 (a).

Quadrupole Triplet. Three consecutive electrostatic quadrupole sets are arranged cylindrically, acting as a dual focal length lens to focus the beam in the x- and y-planes. Refer to Figure 3.3, c) for an illustration.

Quadrupole Deflector. A set of four electrodes that can bend the beam by 90°and simultaneously focuses the beam. The manipulation of the beam using this element is illustrated in figure 3.3, b).

Faraday cup. This element is employed to monitor the current intensity of the beam and it is placed at different points along the beamline. Consists of a metal cup, where a current is measured.

Collimator. A plate with a small slit or hole in the middle that can be set to a voltage to define the beam geometry, or used as a readout.

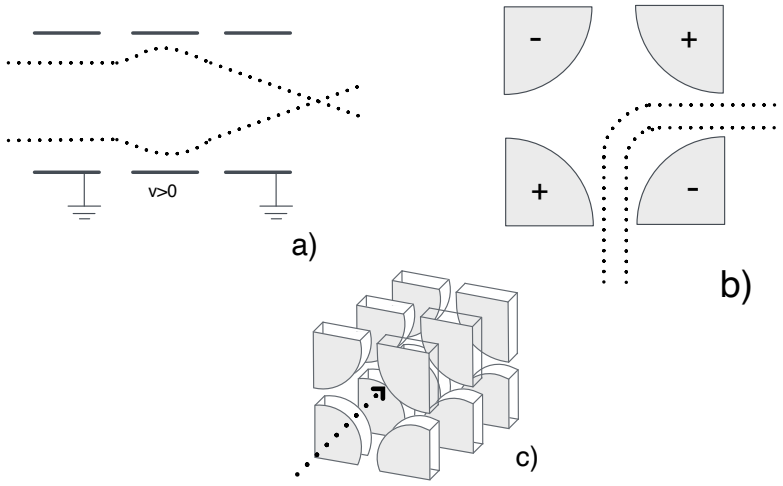

Figure 3.3: Schematics of ion optics elements. a) depicts how a set of einzel lens focuses the ion beam, b) shows the bending of the beam done through a quadrupole deflector and c) illustrates the positioning of a quadrupole triplet against the position of the ion beam. In all three schematics, the ion beam is represented by a dotted line.

3.1.3 Lasers

Within photodetachment experiments, a laser emits coherent and monochromatic light, which is directed towards the ion of interest. When the ion absorbs photons from the laser, the electron within the ion can be excited to a higher energy level or completely detached from the ion. The lasers photon energy must match or exceed the ionization energy of the ion. Throughout the photodetachment studies, the lasers intensity and wavelength is varied by using a two-step excitation process.
One of the laser systems used in this work is a dye-laser, which is a system that uses a diluted dye pumped through a tube to the laser cavity of a pulsed laser. A specific output radiation is then selected in the cavity using an adjustable grating [9].

Another type of laser system used in this work is a Optical Parametric Oscillator (OPO). The working principle of an OPO is based on the parametric interaction of a strong pump wave with a crystal with a large nonlinear susceptibility. In this way, parametric generation splits a pump photon into two photons with different energies while satisfying conservation of energy at every point in the nonlinear crystal. An OPO laser, in general, is pumped by a Q-switched laser source.

In this thesis, an EKSPLA© NT342 series laser [39] was used for resonant excitation and a a Sirah Precision dye laser for the photodetachment process, as described in Chapter 2. The parameters in which the lasers were operated are presented later in the text.

3.1.4 RADAR

This experimental beamline is shown schematically in figure 3.4 and uses Resonant Ionization Spectroscopy (RIS) for the study of negative ions, as described in Section 2.3. The chamber can be described by three elements: a field ionizer, an energy analyzer, and a position-sensitive detector.

The Field Ionizer (FI). It is composed of four individual plates that are biased in an increasing absolute value, until the last plate, where the potential drops to zero.

The Energy Analyzer. Comprised of two curved parallel plates, which are biased to a set potential that can bend the beam and separate the desired species of positive ions by energy. Then, the positive ions are directed towards a position-sensitive detector while the remaining negatives are directed towards a Faraday cup.

Position Sensitive Detector. Following the energy analyzer, a detector comprised of a pair of MicroChannel Plates (MCPs) in a chevron configuration with a delay line anode that allows the collection of information on the impact position of the incoming particles along the impact time; a hit in the anode that is triggered by the MCP produces a pulse with a known initial time (once the hit

is detected) and final time (once it reaches the edge of the wire). Therefore, the pulse position can be obtained from the arrival time difference. As the desired species and background are separated by their difference in kinetic energy, these two can be discerned as they would hit the detector at different positions [40].

In this thesis, RIS is combined with field ionization [36] to achieve a highly sensitive and selective process. This combination works by choosing the corresponding values for the potential administered in the FI accordingly to each experiment, such as the resulting Rydberg atoms pass through the first part of the FI with weak electric field mostly unaltered, to then be field ionized from the strong electric field on the second part of the FI, as depicted in figure 3.5.

In addition, the FI accomplishes the required selectivity separating the diversity of the resulting atoms from the interaction region: the negative ions will be deflected slightly to the left and measured in a Faraday cup, the neutral atoms will follow straightforwardly unaffected by the electric fields, and positive ions produced in the second part of the FI (i.e. the Rydberg atoms) will be decelerated and bent towards the right by the electrostatic analyzer, curving towards one side of the PSD (Position Sensitive Detector) located at the far end, while the positive ions created in the first part of the FI (by collisions) will conserve their initial kinetic energy and consequently, with a larger radius of curvature compared to the first mentioned positive ions, curved towards the PSD in a different section. This separation process is depicted in figure 3.4.

The spatial differences in the hits of the two different types of positive ions differ by a few millimeters, enough to separate the background (i.e. the positive ions produced by non-photon-induced processes such as collisions) and the signal (i.e. the positive ions produced by resonance ionization). The only information extracted from the MCP is the spatial distribution hitting the detector. The signal obtained from the field-ionized Rydberg atoms is directly related to the photodetachment cross section of the atom in a specific state. This threshold is defined by the Wigner Law, which has been previously discussed in the fundamentals chapter.

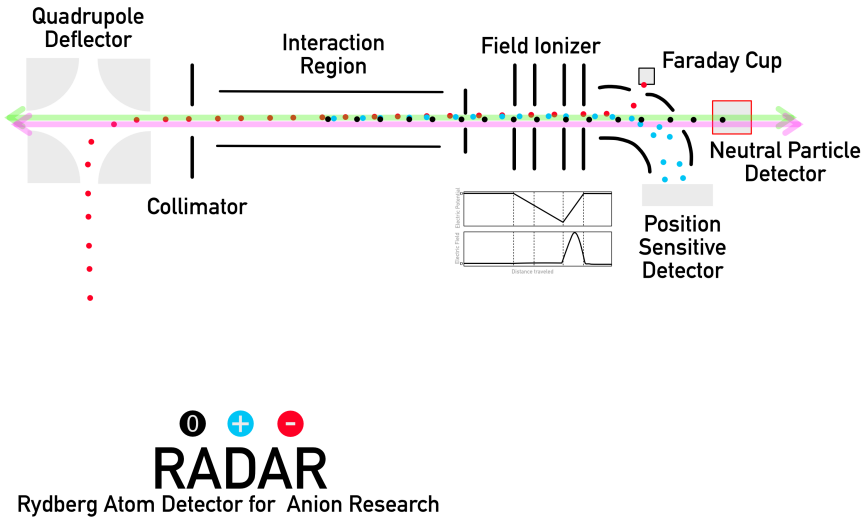

Figure 3.4: Diagram of RADAR. This figure depicts the ion optics used to focus the beam, the four plates from the Field Ionizer and the localization of the constructed NPD at the low end of the chamber. It is also possible to notice the set-up of the lasers, in green and pink. This geometry allows to take measurements in a co- and counterpropagating geometry. The implemented NPD from this work can be seen at the end of the chamber, next to the curved plates.

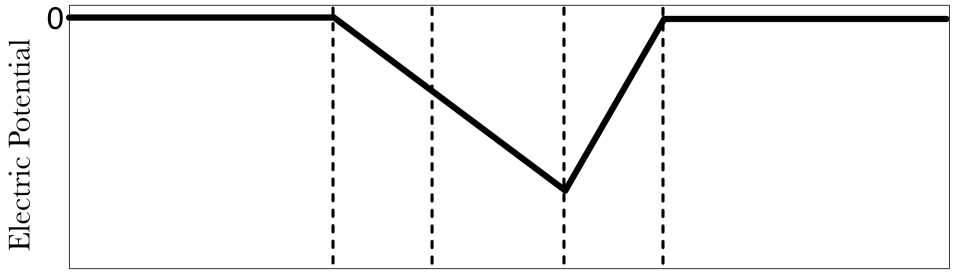

Figure 3.5: Scheme of the electric potential decay and rising, respectively, as an atom travels through the field ionizer.

Chapter 4

The Neutral Particle Detector

4.1 Neutral atom detection

From equation (2.2), it is possible to see that the final products of a photodetachment process are a free electron and a neutral atom. Then, it is natural to set the monitoring of this process by sensing either the electrons or the neutral atoms, or both.

A secondary emission detector grants the possibility of detecting the resulting neutral atoms from any photodetachment experiment if the ratio of a neutral atom impinging on the detector and the produced secondary electrons is known.

4.2 Design

The NPD design required should take several factors in consideration, as described by Hanstorp [11]: The target should be contrived conductive, allowing the generation of secondary emission electrons on impact from the neutral atoms. The geometry should allow, in this case, for laser beams to go through the detector to grant the possibility for collinear geometry experiments (i.e. the overlapping of the laser beam with the ion beam in a copropagating and counterpropagating geometry). These two implications require a material not only conductive, but also transparent to the region of the electromagnetic spectrum where the desired laser works [11].

For the NPD constructed in this work, a single atomic layer of graphene coating a quartz plate is used, as the graphene coating allows the necessary surface conductivity while preserving the quartz characteristic optical transparency to regions from far IR to UV ranges [12, 41]. This plate is referred to as the target.

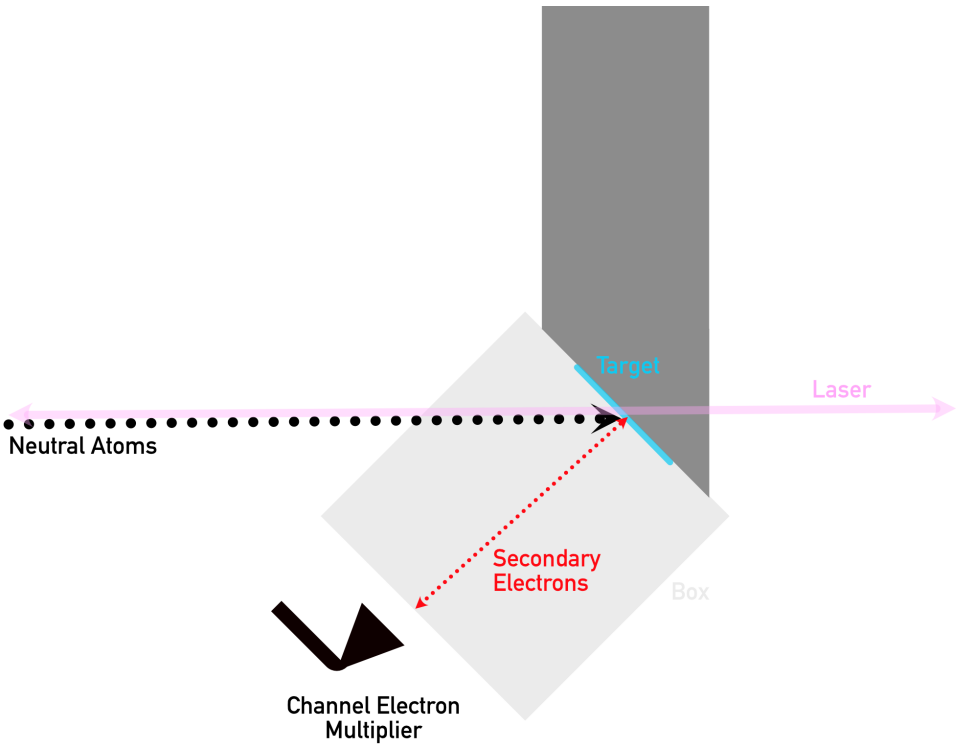

Figure 4.1: Diagram of the NPD design. The neutral atoms (black dotted line) impinge on the surface of the target (blue), where they produce secondary electrons (red) that are guided by the box (light gray) to the CEM, where the signal is collected. The laser (pink) goes through the target, allowing both parallel and anti-parallel geometries.

The space where the detector would be mounted is limited, with the available space being a cylinder inside a chamber of about 9 cm diameter base and 20 cm height. The detector setup involves the use of a box that serves multiple purposes. Firstly, it serves as an entrance orifice to accommodate the significant distance between the neutrals' production point and the detector. Additionally, the box conducts an applied electric potential that acts as a guide for the secondary electrons. These electrons originate from the quartz target and need to be directed towards the Channel Electron Multiplier (CEM) within the detector. For the sake of practicality, Kimball Physics© parts were used. By using these parts, the design was ensured to be symmetrical and easily modifiable, if needed.

Based on the electrical requirements, the mechanical setup was done and the 3D CAD file was created (shown in figure 4.2) using Siemens Parasolid™ Shapr3D software. Subsequently, this file was exported to SIMION©, an ion optical simulation software. This program can calculate 2D and 3D electrostatic and some magnetic fields, including the trajectories of the charged particles through those fields. Its main numerical method for solving the required partial differential equations is Runge-Kutta, mainly the Laplace equation. This software also allows the programming, visualization and data recording for the simulations. More about this software can be read in [42].

Utilizing the known setup of the RADAR chamber, in particular its interaction region, the size and divergence of the neutral beam impinging on the target plate was simulated in order to verify position and size of the NPD. These dimensions are detailed in the results subsection of this chapter. Subsequently, a secondary emission script was written with help of the software's examples and previous simulation [41] and finally implemented to simulate the creation of the secondary electrons. After several tests, the ideal voltages for each section of the detector were determined.

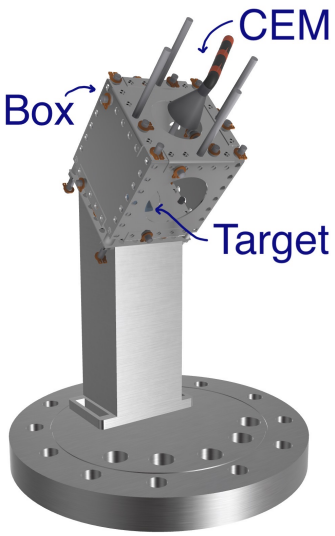

Figure 4.2: 3D CAD Model designed for the NPD detector.

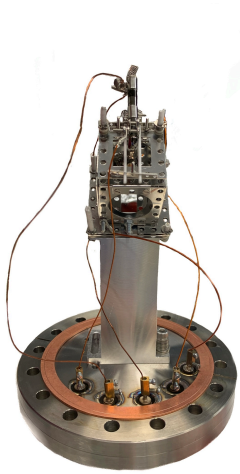

Figure 4.3: Final assembly of the NPD. The detector is shown upside down.

4.3 Results

The simulation resulting from the integration of the CAD file to the ion trajectory software is illustrated in figure 4.4.

Figure 4.4: Simulation of neutral atoms (shown in pink) emerging from right to left from the interaction region, through the Field Ionizer and up to the NPD. The impacts of the ions are depicted in red and the secondary emitted electrons are displayed in blue.

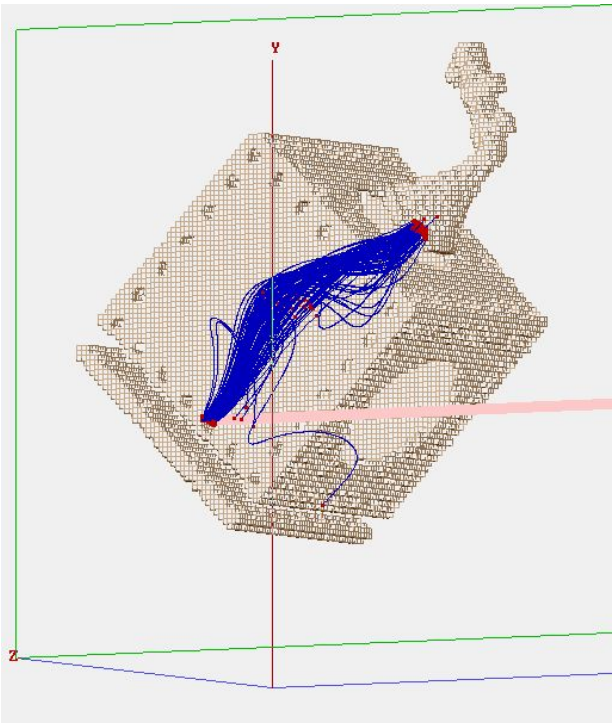

Figure 4.5: Close up of the simulation of the ion beam trajectory and the resulting secondary electrons using SIMION©. The neutral atoms (pink) impinges on the target (red), where the secondary electrons (blue) are guided with an electric field applied from the detector box, to the CEM, where the signal is collected (red).

From the SIMION© simulations and the CEM testing mentioned above, the voltages determined to be the ideal for the detector are shown in table 4.1.

Two tests were done to ensure that the NPD is working as expected. First, to revise the optimal functionality of the selected CEM and finally, to use a laser to test the entire detector.

Element	Voltage [V]
Target	-150
Box	-50
CEM	2000

Table 4.1: Ideal voltages for the designed NPD.

Once the assembly according to the 3D CAD simulations was done, the detector was placed in the chamber and pumped down to pressure of the order of 1×10^{-6} mbar, which is marked as the working pressure of a CEM, according to the manufacturer [43]. After the pressure reached the desired values, small steps of 100 V were applied to the CEM, until a signal resulting from background arose at an applied 2000 V as depicted in figure 4.6.

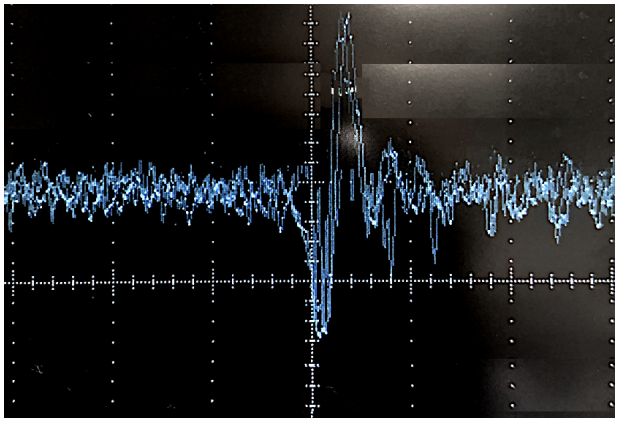

Figure 4.6: Picture of the result on the CEM testing. The voltage applied to the CEM was 2000 V. The small steps mentioned before were progressively applied until a rise in the oscilloscope was found. This rise indicated a signal detection from the CEM. This exercise allows the diagnostic of the current CEM in use and the familiarization of the values needed for its operation, which is a crucial part for further testing of the NPD.

The NPD was subjected to a test with an OPO laser from EKSPLA©, model NT342 [39] to determine its functionality in terms of secondary emission detection. The laser was tuned to different wavelengths and the counts were acquired over a period of 10 s, 20 periods each wavelength. The resulting counts are normalized by laser power, obtaining figure 4.8. With the help of an oscilloscope, the variations of the signal when applying the box and target voltages where observed, as shown in figure 4.7. The increased count rate as the laser wavelength is tuned to lower wavelength can be explained due to deviation of the laser path, the approximation to the work function of the material of the chamber (i.e. Aluminium) [44], higher photon energy that results in a higher photoelectron current or saturation of the CEM. This rise in count rate is to be avoided during the testing, as it can result in an overload to the CEM and therefore, a disabling of the NPD. The threshold for the work function of aluminum is known to be at 4.5 ± 0.5 eV [45], and therefore it is clear to see from figure 4.7 that these tests were performed at much lower energy than this threshold.

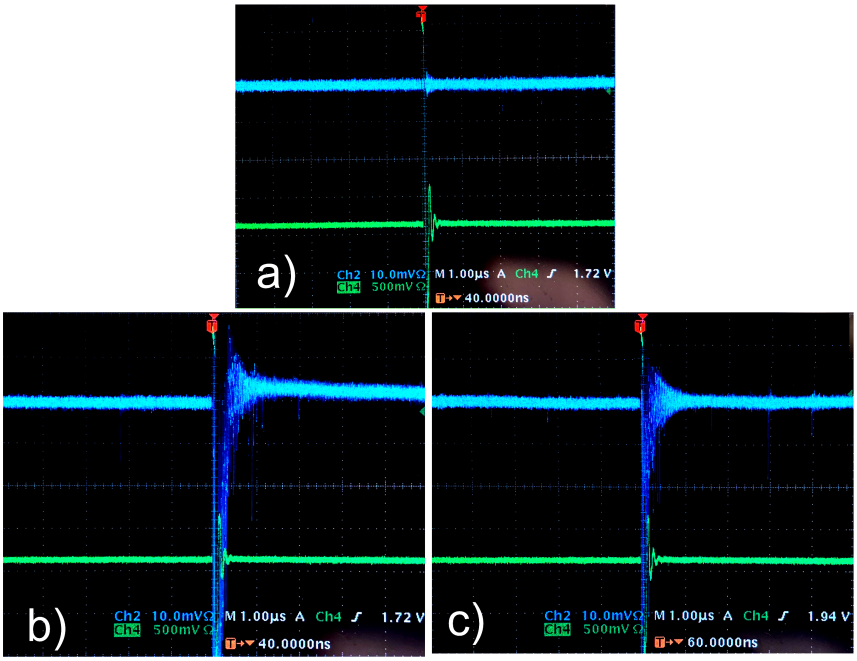

Figure 4.7: Illustration of the results of the application of the voltages from the box and the target in the NPD. **a)**The CEM has no voltage applied. **b)**the CEM has voltage applied, with no voltage on the box and target. **c)** Both the CEM, the box and target have voltages applied. It's clear to see that the effect of the voltages in the NPD acts as a filter on the CEM. Channel 1 (blue) indicates the signal collected from the CEM, while channel 2 (green) indicates the laser signal collected from a photodiode, which was placed along the laser optical path. Both channels had their own scale adjusted in order to show both signals in a clear way. In each picture, the bottom line shows the parameters on the position and time scales for each channel.

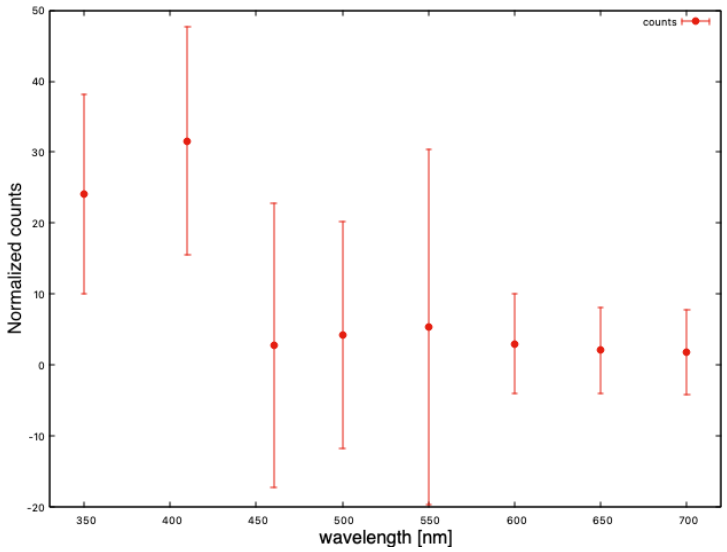

Figure 4.8: Detected photoelectron counts dependent of laser wavelength. The counts are normalized to the lasers output power. This testing process was done inside GUNILLA.

Chapter 5

The testing chamber

5.1 Motivation

Most of the detectors and components used in GUNILLA are tested inside the main apparatus, implying a considerable amount of beam-time invested in these evaluations.
By constructing a test chamber that resembles the conditions from the main GUNILLA device but independent from its vacuum pumping and significantly smaller in size, it will be possible to optimize the beam time needed to run the experiments. Then, the testing of components can be done simultaneously with Laser PhotoDetachment (LPD) experiments without interfering. Hence, a test chamber with an electron gun was designed, to allow testing of CEMs and other detectors.

5.2 Working principle

By utilizing a LaB_6 cathode as an electron emitter with a known emission rate, it is possible to create an electron gun. The electron beam is shaped and accelerated by placing an anode immediately after the emitter, resulting in a stable stream of electrons. This electron beam can be further manipulated and employed for testing various optical elements, since the emission rate is known and the beam current can be measured. When a material is heated and the thermal energy surpasses its work function, electrons are liberated from the material or electrode, forming an electron current. This phenomena is called **thermionic emission**. This was first reported by Edmond Becquerel in 1853 [46]. The emitted current density of the cathode, J, is given by the Richardson-Dushman equation [47]

$$J = AT^2 exp(\frac{-W}{kT}), \tag{5.1}$$

where T is the temperature of the emitter. W is the work function of the material, k is the Boltzmann constant, and A is known as the Richardson constant. This phenomenon is the basis for electron gun

designs.

5.3 Design

A beam was generated using a LaB_6 Denka© source, with the emitted electrons then guided by an anode plate to shape them into a coherent beam. To facilitate beam manipulation, a steering box was incorporated consisting of a set of electrodes arranged in a specific configuration, often with adjustable voltages applied to them. By varying these voltages, the steering box can generate electric fields that alter the paths of ions passing through it, allowing for precise alignment and bending to different positions. Within the beam path, a plate with a pinhole served a dual purpose. It could function as a collimator, ensuring a well-defined and focused beam, or as a reading element, providing a means to monitor the beam intensity. Finally, an Einzel Lens was integrated into the setup to further enhance beam focus. The source itself consists of clamped Kimball Physics© plates, with one plate point-welded to a ring situated inside the chamber. This arrangement ensured stability and proper positioning. Immediately following the clamped plates, another plate with a smaller inner circle acted as the anode, responsible for effectively shaping the emitted electrons into a coherent beam. The order of these elements can be seen in figure 5.1.

The optic elements are held by another Kimball Physics© plate attached to the flange, where four ceramic rods hold the next element, an electrically isolated steering box. On the other side of the chamber, an Einzel lens is sitting in a mount whose prototype was built in a 3D ZYYX Labs classic printer with PolyLactic Acid (PLA) material, using the predetermined settings from the printer's software. These mounts were designed to allow each 1 cm wide ring to be electrically supplied and held in place. Each mount is stacked one over the other, keeping a 1cm distance between rings. A fourth mount is added, with the slight variation of the holding. This mount is modified to hold and supply another Kimball Physics© plate, which acts as a collimator. Even though this is initially intended just as a readout, a voltage can be applied to the collimator to endorse further focusing of the beam.

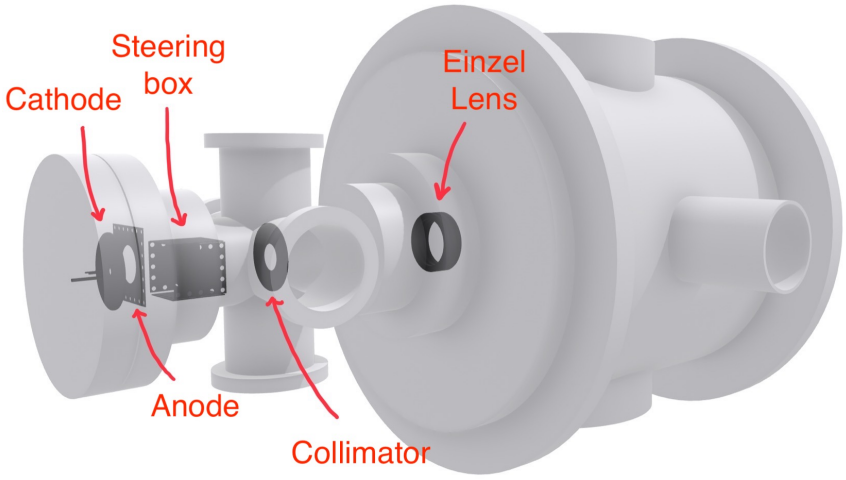

Figure 5.1: 3D visualisation with the optics included. From left to right, the cathode, anode, steering box, collimator and einzel lenses can be observed in darkest gray.

5.4 Simulations

Some simulations were done using the 3D CAD model for the test chamber, using SIMION©. The configuration of the emitting source was set according to the description on the performance of this cathode from the Denka© manual [48]. Considering an emitted beam around 8×10^{-11} A at 1500°C according to the manual [48], the simulations were made, applying different voltages to the elements so that the emitted electrons form a stable beam that can be manipulated and bent by the steering box, all the way to the target element to be tested.

From these simulations, the ideal voltages for the optics elements considering a 1 KeV beam are shown in 5.1.

The future construction of this chamber will be based on these preliminary results.

Element	Voltage [V]
Anode	-1000
Plate of steering box	Up to 500
Middle EL ring	1000
External EL rings	0

Table 5.1: Table of ideal voltages for the designed optics on the testing chamber. The voltages on the plates of the steering box depend on the direction in which the beam is to be bend, and even though it's not necessary, an anti-symmetrical effect is recommended on the opposite plate (i.e. apply the same voltage but negative.) to avoid divergence on the beam.

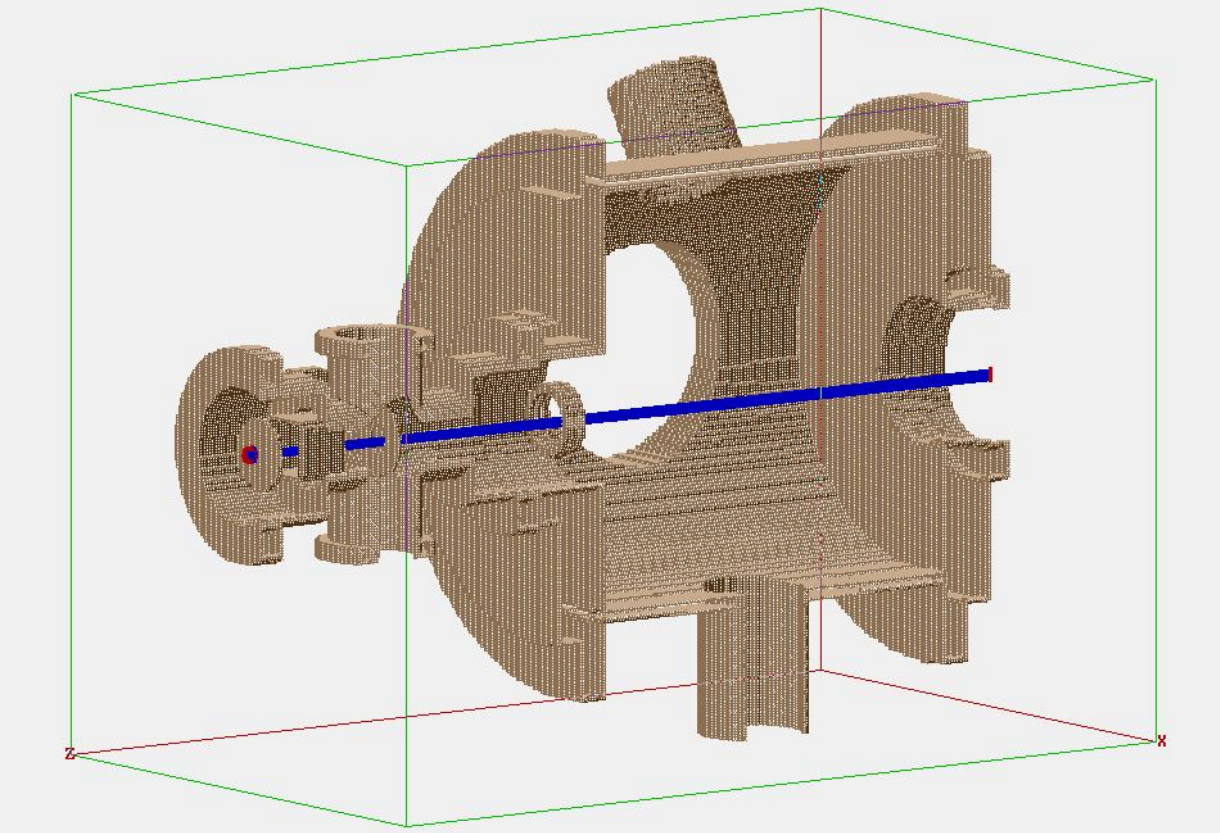

Figure 5.2: Simulation of the testing chamber with SIMION©. From left to right, the first red spot indicates the electron surge from the cathodes, which follow the path depicted in blue to finally hit on the opposite side of the chamber, depicted again in red. The main chamber as well as the optical elements are portrayed in brown.

Chapter 6

The Electron Affinity of Rubidium

The study of negative ions is highly relevant, as mentioned in Chapter 1 of this work, and the specific study of alkali negative ions was shown to be of particular interest after the discovery of a resonance below the $^2P_{1/2}$ threshold [49]. After several years, alkali threshold resonances were confirmed [50] specifically in Cs^- and a similar but weaker behavior was predicted for Rb. Thus far, the most precise value experimentally measured for the EA of Rb was determined in 1978 as 485.915(21) meV from a measurement detaching into the $^2P_{1/2}$ state [51]. One of the most recently performed experiments at GUNILLA was to measure and offer an updated value for the EA of rubidium with high precision. The use of RADAR to perform this experiment allows the implementation of the RIS technique for ^{85}Rb atoms, as explained in Section 2.3.

A copper cathode (later replaced by aluminum) with Rb and Ag lightly pressed powder was prepared and inserted into the Cs sputter ion source, producing a beam of negative Rb ions, which was aligned into the RADAR spectrometer where an average current of 20 pA of ^{85}Rb was measured, as shown in figure 6.1.

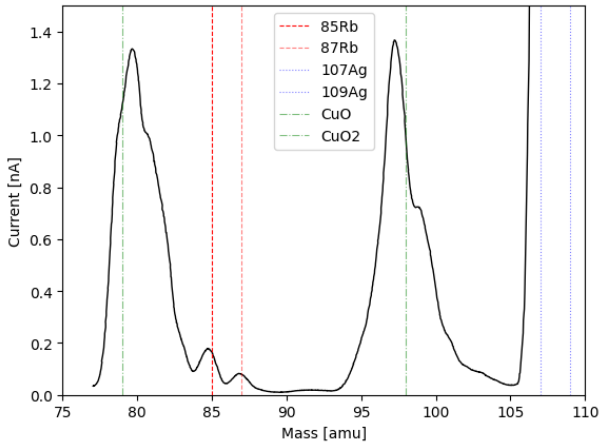

Figure 6.1: Mass Spectra of the ion beam. The presence of the element of interest (^{85}Rb) is shown in red, along with other elements such as silver and copper oxides, present due to the cathode formula mixing and residual interactions [52].

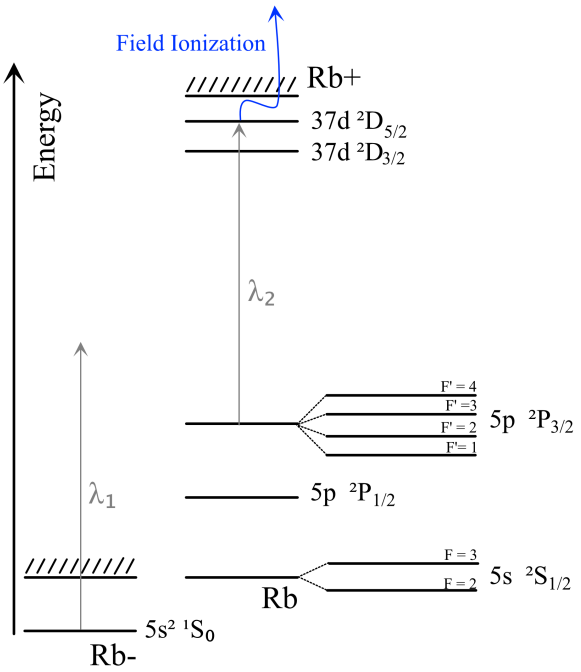

Figure 6.2: The (not to scale) energy diagram of Rb and Rb^-. A negative Rb ion absorbs a photon λ_1 that excites it to an intermediate excited state or to the ground state. Immediately, a second photon λ_2 is administered, further exciting the ion to a Rydberg state from which the ion is field ionized.

6.1 Data acquisition triggering

To improve the signal-to-background ratio, a data compilation system was employed. This system involved continuous monitoring of various parameters, such as laser power output, ion current, and wavelength for both lasers. Additionally, an externally triggered time-acquisition lapse was implemented for the PSD. This enables the extraction of the desired signal while minimizing unwanted background noise. By averaging these three factors for each data point, the signal could be effectively normalized during the analysis of results at different photon energy values. The experiment acquisition time window was established at approximately 30s, matching the ions' time-of-flight from the interaction region to the detector.

6.2 Particle Detection

As explained earlier, the difference between the signal and background is represented by the spatial difference. Accurately pinpointing the spatial zone in the MCP where the received hits correspond to the desired signal is crucial.

After evaluating the hit patterns in the software, a Region of Interest (ROI) is selected based on hits that are identified as originating from the ion beam interaction with the laser. This interaction is determined by comparing hit counts with and without laser interaction in the software, as depicted in figure 6.3. Once the region of interest has been identified, it is centered and the count is focused on the RoI.

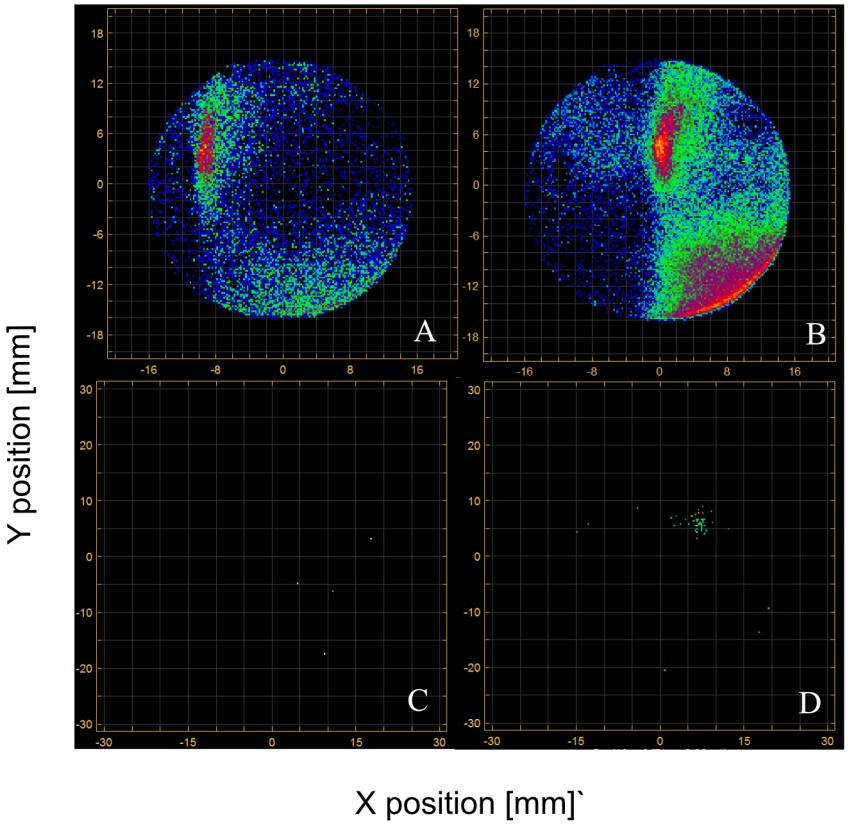

Figure 6.3: MCP signal detection. This diagram showcases the distinctions between an ion beam with and without laser interaction. Panels A and B display the comprehensive detection of MCP hits, with A depicting no laser interaction and contrasting with B, which exhibits hits with laser interaction. Panels C and D highlight the selected Region of Interest (RoI), which concentrates on the area that exhibits the highest activity in B compared to A. C represents hits with no laser interaction, while D represents hits with laser interaction.

6.3 Laser conditions

For accurate particle detection, the lasers utilized in this experiment must satisfy specific conditions. These conditions ensure the desired excitation state of ions while preventing unintended processes like two-photon excitation, as previously discussed in the fundamentals section (illustrated as symbols λ_1 and λ_2 in figure 6.2).

Both lasers were precisely timed with a few nanoseconds interval, dependent on the propagation geometry, to optimize the excited state population. The experimental setup featured a Sirah PrecisionScan dye laser and an EKSPLA OPO laser, both pumped by a 10 Hz Nd:YAG pulsed laser.

The initial laser, a dye laser, was used for photodetachment and operated within a 518-614 nm range using Rhodamine B. It produced a pulse energy of about 0.5 mJ, measured at RADAR chamber exit. The

subsequent laser, an OPO, facilitated resonant ionization and possessed a bandwidth of around 90 GHz.

Saturation occurs when the stimulated emission rate equals the photon absorption rate, and is simultaneously greater than the spontaneous emission rate of a photon. Power broadening occurs when the laser saturates the induced transition, causing a nonlinear behavior. To counter these effects, the OPO laser's pulse energy was reduced to approximately 50 μJ, and the dye laser's frequency was recorded using a HighFinesse wavelength meter (WS-6). This meter was daily calibrated via saturated absorption spectroscopy of rubidium gas in a low-pressure quartz cell, ensuring precise measurements.

6.4 The Electron Affinity of Rb

6.4.1 Threshold measurement

A typical Wigner threshold behavior with an s-wave detachment is expected for the measurements of the partial cross section of Rb^-. This partial cross section is measured in co- and counterpropagating ion-laser geometries, as explained in section 2.3.1 and illustrated in figure 3.4. The threshold was then determined by fitting the obtained data in accordance with equation (2.8). For each point, an average of the ion beam and laser power was calculated, including the standard deviation. The corresponding signal in the count rate was normalized to both ion beam current and laser power, and the propagation of the error from the standard deviation and propagated the uncertainty as

$$\sigma = \sqrt{(\frac{\partial f}{\partial s})^2 + (\frac{\partial f}{\partial c})^2 + (\frac{\partial f}{\partial p})^2}\,, \tag{6.1}$$

with count rate (s), ion current (c) and laser power (p). For each scan, a plot of the relative cross section as a function of photon energy threshold was obtained, which was fitted as described before. The average over all the analyzed thresholds resulted in a final value for the threshold onset of 2.074 947 6(8) eV. Figure 6.4 displays the results of the red Doppler shift correction, incorporating both counter- and copropagating scans.

6.4.2 Electron Affinity calculation

The threshold onset for each two scans was computed using the geometric mean value in both co- and counterpropagating geometries. These onset values were then averaged to obtain a single threshold value after correcting for the Doppler shift. Subsequently, according to [53], the energy difference between ^5S and $^5P_{3/2}$ was taken as 12 826.545 cm^{-1} or 1.589 049 06(25) eV. The error bars in the figure represent the standard deviation, and systematic errors were not taken into account for the uncertainty. These systematic errors can arise from factors such as laser linewidth and/or laser-ion beam overlap. The energy

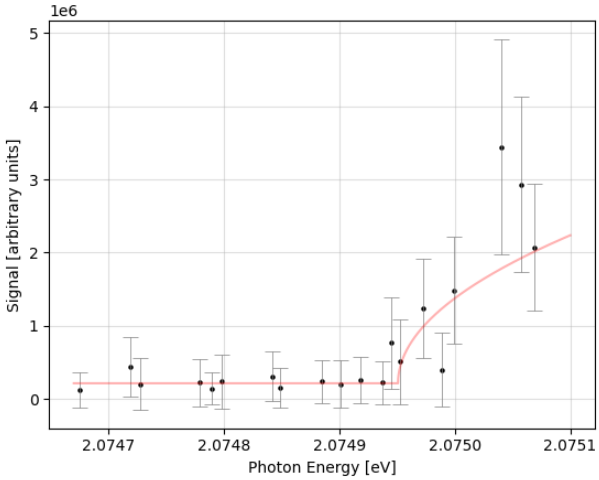

Figure 6.4: Plot showing the red Doppler shift correction for a scan and illustrating the threshold onset. The fit can be appreciated in a solid red line.

difference was then subtracted from the previously mentioned threshold value, resulting in the experimental determination of the electron affinity of Rb as 485.894(8) meV.

In previous experiments, the most precise value obtained for the electron affinity was reported by Frey, Breyer, *et al.* in 1978 [51] with a value of 0.485 940(44) eV. This value was determined by LPD spectroscopy.

It is clear that the value obtained in this experiment and the previous measurement by Frey *et al.* are in agreement. The RIS application granted the possibility of exclusively selecting the desired $^5P_{3/2}$, which is known to exhibit an s-wave threshold behavior. The inclusion of this technique contributed to enhancing precision by an order of magnitude over previously cited measurements.

Chapter 7

Conclusion

The main work presented in this thesis concerned the construction of a neutral particle detector for experiments on spectroscopy of negative ions, particularly in photodetachment experiments. The implementation of this detector will help in a variety of ways, such as a secondary emission detector that has a higher sensitivity in beam current reading compared with the typical methods used, for example, a Faraday cup.
Combined with the signals obtained from the position sensitive detector, this NPD gives a broader range of possible experiments to perform in RADAR, improving the monitoring of the photodetachment process. An initial test confirmed the proper functioning of the NPD, which will be subsequently integrated and extensively tested in future LPTS experiments. In future experiments, this will open up the possibility of using RADAR as the main beamline for all photodetachment experiments.

For the second part of this work, the design of a testing chamber was presented. This chamber offers a practical solution regarding an important part of any experimental setup: the process of testing the elements that are needed during the experiment. For immediate action, the chamber was designed to have a source that produces an electron beam and accommodates channel electron multipliers to evaluate electron gain, especially after rigorous use or any aging processes.

For future experiments, the versatility of the design of this chamber will allow the source to be modified according to the testing requirements. The presented design is ready to be considered for construction with the given theoretical values from table 5.1.

In the last part of this study, the EA of ^{85}Rb was determined to be 485.894(8) meV. Although the obtained value is in good agreement with one value previously obtained from [51], further considerations can be taken to achieve a more precise value, such as the convolution of the laser linewidth, velocity shift, or systematic errors from the laser and ion beam overlap. A more detailed article about this experiment

is to be published [54].

In the future, the same method described in chapter 6 can be applied to study the EA of other elements such as francium (Fr). This is the heaviest known alkalide, which presents no stable isotopes and whose EA has not been experimentally determined. The EA of Fr was theoretically calculated as 0.491(5)eV [55]. The EA value can be measured in radioactive facilities, such as CERN-ISOLDE [56].

Bibliography

[1] J.J. Thomson. Rays of positive electricity. *Proceedings of the Royal Society of London. Series A, Containing Papers of a Mathematical and Physical Character*, 89(607):1–20, 8 1913.

[2] H.S.W. Massey. *Negative Ions*. Cambridge University Press, London, 1 edition, 1938.

[3] Wade L. Fite. Production of Negative Ions and Noise in Negative Ion Beams. *Physical Review*, 89(2):411–415, 1 1953.

[4] L M Branscomb and S Smith. Electron Affinity of Atomic Oxygen. *Physical Review*, 98(4):1127–1128, 5 1955.

[5] L. M. Branscomb and S. Smith. Experimental Cross Section for Photodetachment of Electrons from H- and D-. *Physical Review*, 98(4):1028–1034, 5 1955.

[6] Boris Smirnov. *Physics of Atoms and Ions*. Springer, 2003.

[7] A. O. Lindahl, J. Rohlén, H. Hultgren, I. Yu. Kiyan, D. J. Pegg, C. W. Walter, and D. Hanstorp. Threshold Photodetachment in a Repulsive Potential. *Physical Review Letters*, 108(3):033004, 1 2012.

[8] Eugene P. Wigner. On the Behavior of Cross Sections Near Thresholds. *Physical Review*, 73(9):1002–1009, 5 1948.

[9] Pontus Andersson. *Laser Photodetachment of Negative Ions*. PhD thesis, University of Gothenburg, Gothenburg, Sweden, 2009.

[10] P. Mahadevan, G. D. Magnuson, J. K. Layton, and C. E. Carlston. Secondary-Electron Emission from Molybdenum Due to Positive and Negative Ions of Atmospheric Gases. *Physical Review*, 140(4A):A1407–A1412, 11 1965.

[11] D. Hanstorp. A secondary emission detector capable of preventing detection of the photoelectric effect induced by pulsed lasers. *Measurement Science and Technology*, 3(5), 1992.

[12] J. Warbinek, D. Leimbach, D. Lu, K. Wendt, D. J. Pegg, A. Yurgens, D. Hanstorp, and J. Welander. A graphene-based neutral particle detector. *Applied Physics Letters*, 114(6), 2019.

[13] José Navarro. An Experimental Determination of the Electron Affinity of Cesium. Master's thesis, University of Gothenburg, Gothenburg, 2019.

[14] J Warbinek. *Spectroscopy of Negative Ions*. Master's thesis, University of Gothenburg, Gothenburg, 4 2020.

[15] Christophe Blondel, Christian Delsart, and François Dulieu. The photodetachment microscope. *Physical Review Letters*, 77, 1996.

[16] C Blondel, W Chaibi, C Delsart, and C Drag. The fine structure of s and s measured with the photodetachment microscope. *Journal of Physics B: Atomic, Molecular and Optical Physics*, 39, 2006.

[17] H. T. Schmidt and R. D. Thomas. First storage of ion beams in the double electrostatic ion-ring experiment: Desiree. *Review of Scientific Instruments*, 84, 2013.

[18] Moa K. Kristiansson and Kiattichart Chartkunchand. High-precision electron affinity of oxygen. *Nature Communications*, 13, 2022.

[19] T. Andersen, H. K. Haugen, and H. Hotop. Binding Energies in Atomic Negative Ions: III. *Journal of Physical and Chemical Reference Data*, 28(6):1511–1533, 11 1999.

[20] Chuangang Ning and Yuzhu Lu. Electron Affinities of Atoms and Structures of Atomic Negative Ions. *Journal of Physical and Chemical Reference Data*, 51(2):021502, 6 2022.

[21] Rulin Tang, Yuzhu Lu, Hongtao Liu, and Chuangang Ning. Electron affinity of uranium and bound states of opposite parity in its anion. *Physical Review A*, 103:L050801, 5 2021.

[22] Chuangang Ning and Yuzhu Lu. Electron affinities of atoms and structures of atomic negative ions. *Journal of Physical and Chemical Reference Data*, 51:021502, 6 2022.

[23] Ryan C. Fortenberry. Interstellar Anions: The Role of Quantum Chemistry. *The Journal of Physical Chemistry A*, 119(39):9941–9953, 10 2015.

[24] Thomas J. Millar, Catherine Walsh, and Thomas A. Field. Negative Ions in Space. *Chemical Reviews*, 117(3):1765–1795, 2 2017.

[25] Alexander Grigoriev. *The neutral particle detector on the Mars and Venus Express missions*. Swedish Institute of Space Physics, 2007.

[26] Ralf I. Kaiser and Nils Hansen. An Aromatic Universe–A Physical Chemistry Perspective. *The Journal of Physical Chemistry A*, 125(18):3826–3840, 5 2021.

[27] D. Leimbach and *et al.* The electron affinity of astatine. *Nature Communications*, 11:3824, 7 2020.

[28] J M Zhang and Y Liu. Fermi's golden rule: its derivation and breakdown by an ideal model. *European Journal of Physics*, 37(6):065406, oct 2016.

[29] Demtröder Wolfgang. *Laser Spectroscopy: Basic concepts and Instrumentation*. Springer-Verlag, Berlin, second edition edition, 1981.

[30] P. Juncar, C. R. Bingham, J. A. Bounds, D. J. Pegg, H. K. Carter, R. L. Mlekodaj, and J. D. Cole. New Method to Measure the Relativistic Doppler Shift: First Results and a Proposal. *Physical Review Letters*, 54(1):11–13, 1 1985.

[31] David Leimbach. *Radioactive negative ions: Production and laser spectroscopy at ISOLDE*. PhD thesis, Johannes Gutenberg-Universität Mainz, Geneva, 5 2021.

[32] G. S. Hurst, M. G. Payne, M. H. Nayfeh, J. P. Judish, and E. B. Wagner. Saturated Two-Photon Resonance Ionization. *Physical Review Letters*, 35(2):82–85, 7 1975.

[33] V. V. Petrunin, H. H. Andersen, P. Balling, P. Kristensen, and T. Andersen. Resonance ionization spectroscopy of negative ions. pages 103–108, 1997.

[34] T. Andersen. New approaches to negative ions: resonant ionization spectroscopy and storage rings. *Nuclear Instruments and Methods in Physics Research Section B: Beam Interactions with Materials and Atoms*, 123(1-4):508–514, 3 1997.

[35] Michael Savina and Reto Trappitsch. *Resonance ionization mass spectroscopy (RIMS): Fundamentals and applicatoions including secondary neutral mass spectrometry*. Wiley Online Library, 2021.

[36] J. Welander, J. Navarro Navarrete, J. Rohlén, T. Leopold, R. D. Thomas, D. J. Pegg, and D. Hanstorp. A field ionizer for photodetachment studies of negative ions. *Review of Scientific Instruments*, 93(6):065004, 6 2022.

[37] J Parks and N Omenetto. *International Symposium on Resonance Ionization Spectroscopy and Its Applications*, volume 1. Institute of Physics, Bristol, Philadelphia, 9 1990.

[38] R. Middleton. A review of ion sources for accelerator mass spectrometry. *Nuclear Instruments and Methods in Physics Research Section B: Beam Interactions with Materials and Atoms*, 5:193–199, 11 1984.

[39] EKSPLA. UniPG EKSPLA Laser Manual. Technical report, Lithuania.

[40] RoentDek Handels GmbH. RoentDek MCP Delay line manual. Technical report, Frankfurt.

[41] Jessica Warbinek. Investigation of the photoelectric effect in Graphene and ITO in a Neutral Particle Detector. Master's thesis, University of Gothenburg, Gothenburg, 2 2018.

[42] David Dahl. SIMION. `https://simion.com/info/simion.html`, 2004.

[43] Burle Photonis. Channel Electron Multiplier handbook for Mass Spectrometry applications.

[44] Edgar Mitchell and John Mitchell. The work functions of copper, silver and aluminium. *Proceedings of the Royal Society of London. Series A. Mathematical and Physical Sciences*, 210(1100):70–84, 12 1951.

[45] Michael C. James, Mattia Cattelan, Neil A. Fox, Rui F. Silva, Ricardo M. Silva, and Paul W. May. Experimental studies of electron affinity and work function from aluminium on oxidized diamond (100) and (111) surfaces. *Physica Status Solidi (B) Basic Research*, 258, 2021.

[46] Edmond Becquerel. "reserches sur la conductibilité électrique des gaz à des températures élevées" [researches on the electrical conductivity of gases at high temperatures]. *Comptes rendus hebdomadaires des séances de l'Académie des sciences*, 1853.

[47] Saul Dushman. Electron emission from metals as a function of temperature. *Physical Review*, 21, 1923.

[48] Denka. Denka LaB6 CATHODE Manual. Technical report, Japan, 2001.

[49] T. A. Patterson, H. Hotop, A. Kasdan, D. W. Norcross, and W. C. Lineberger. Resonances in alkali negative-ion photodetachment and electron affinities of the corresponding neutrals. *Physical Review Letters*, 32(5), 1974.

[50] M. Scheer, J. Thgersen, R. C. Bilodeau, C. A. Brodie, H. K. Haugen, H. H. Andersen, P. Kristensen, and T. Andersen. Experimental evidence that the 6s6p3PJ states of Cs are shape resonances. *Physical Review Letters*, 80(4), 1998.

[51] P Frey, F Breyer, and H Holop. High resolution photodetachment from the rubidium negative ion around the Rb (5p1/2) threshold. *Journal of Physics B: Atomic and Molecular Physics*, 11(19):L589–L594, 10 1978.

[52] Roy Middleton. *A negative Ion cookbook*. University of Pennsylvania, 1989.

[53] Ingmar Johansson. Spectra of the alkali metals in the lead-sulphide region. *ARKIV FOR FYSIK*, 20(135):1–2, 1961.

[54] A. Ringvall-Moberg and **et al.** The electron affinity of rubidium: A state selective measurement. *J. Phys. B: Atom. Mol. Phys.* ***To be Published***, 2024.

[55] Arie Landau, Ephraim Eliav, Yasuyuki Ishikawa, and Uzi Kaldor. Benchmark calculations of electron affinities of the alkali atoms sodium to eka-francium (element 119). *Journal of Chemical Physics*, 115(6), 2001.

[56] R. Catherall, W. Andreazza, M. Breitenfeldt, A. Dorsival, G. J. Focker, T. P. Gharsa, T. J. Giles, J. L. Grenard, F. Locci, P. Martins, S. Marzari, J. Schipper, A. Shornikov, and T. Stora. The ISOLDE facility. *Journal of Physics G: Nuclear and Particle Physics*, 44(9), 2017.